Journal of Inorganic and General Chemistry
ZAAC
Zeitschrift für anorganische und allgemeine Chemie

DOI: 10.1002/zaac.202000409

ARTICLE

Running in the Family: Molecular Factors controlling Spin Crossover of Iron(II) Complexes with Schiff-base like Ligands

Sophie Schönfeld,[a] Wolfgang Bauer+,[a] Sebastian Thallmair+,[a, b] Gerald Hörner,*[a] and Birgit Weber*[a]

Dedicated to Professor Dr. Peter Klüfers on the Occasion of his 70th Birthday

Tailoring of spin state energetics of transition metal complexes and even the correct prediction of the resulting spin state is still a challenging task, both for the experimentalist and the theoretician. Apart from the complexity in the solid state imposed by packing effects, molecular factors of the spin state ordering are required to be identified and quantified on equal rights. In this work we experimentally record the spin states and SCO energies within an eight-member substitution-series of N_4O_2 ligated iron(II) complexes both in the solid state (SQUID magnetometry and single-crystal X-ray crystallography) and in solution (VT-NMR). The experimental survey is complemented by exhaustive theoretical modelling of the molecular and electronic structure of the open-chain N_4O_2 family and its macrocyclic N_6 congeners through density-functional theory methods. Ligand topology is identified as the leading factor defining ground-state multiplicity of the corresponding iron(II) complexes. Invariably the low-spin state is sterically trapped in the macrocycles, whereas subtle substitution effects allow for a molecular fine tuning of the spin state in the open-chain ligands. Factorization of computed relative SCO energies holds promise for directed design of future SCO systems.

Introduction

The electronic state of transition metal complexes from the 3d row can be often shuttled between the low spin (LS) and high spin (HS) formulation of octahedral $3d^4$–d^7 configurations. The phenomenon coined as spin crossover (SCO) relates an abrupt change in magnetism with similarly sharp changes in spectroscopic markers and of the metrics of the inner coordination sphere, reflecting the electron count in antibonding metal-borne orbitals. Controlled turnover among spin states through external physical stimuli has been reported in a large number of cases. The most prominent example constitutes octahedral complexes of iron(II), where SCO gives sharp contrast between the diamagnetic LS and paramagnetic HS forms.[1]

In spite of the vast literature on iron(II)-borne SCO, however, the reliable prediction of the parameters that govern the phenomenon – qualitatively and quantitatively – has remained a challenging task. Particularly in the solid state, the molecule-inherent properties can be and in fact are often overridden by packing effects.[2] A salient example for this complexity with a direct bearing on the present work is provided in a recent study on SCO of iron(II) coordination polymers. Based on an invariant $N_2O_2^{2-}$ planar ligating platform (Scheme 1), the derived polymers {[Fe**8**(py∪py)]}$_n$ show remarkably variable SCO in the solid state, when the axial bridging bipyridine ligand py∪py is varied.[3] While 4,4′-bipyridine as a bridge supports a LS polymer up to 400 K, the equally linear bridge 1,2-bis(4-pyridyl)ethyne traps the HS state even at lowest temperatures. Clearly, such massive differences cannot be associated with the very minor (if

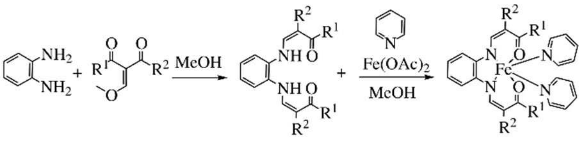

	1	2	3	4	5	6	7	8
R^1	CH_3	CH_3	COEt	COEt	CH_3	Ph	CH_3	CF_3
R^2	CO_2Et	COMe	CO_2Et	CN	COPh	CO_2Et	CO_2Me	CO_2Et

Scheme 1. Synthesis of the ligand family H_2L and the iron(II) complexes [Fe**X**(py)$_2$]; general structure with notation of the substitution pattern.

---

[a] S. Schönfeld, Dr. W. Bauer,+ Dr. S. Thallmair,+ Dr. G. Hörner,
Prof. Dr. B. Weber
Department of Chemistry
University of Bayreuth
Universitätsstraße 30, NWI, 95440 Bayreuth, Germany
E-mail: gerald.hoerner@uni-bayreuth.de
weber@uni-bayreuth.de
[b] Dr. S. Thallmair+
Present address: Frankfurt Institute for Advanced Studies, Ruth-Moufang-Straße 1, 60438 Frankfurt am Main, Germany

[+] The practical work was done at the Department of Chemistry, LMU Munich, Germany.

Supporting information for this article is available on the WWW under https://doi.org/10.1002/zaac.202000409

any) variations in the ligand-field imposed by the axial ligands; they are governed by packing effects, which are currently beyond control, not to say rational design.[4]

By contrast, mutual supramolecular feedback among the SCO units can be largely ruled out, when isolated complexes are studied in solution. In solution (predominantly) the inherent molecular properties are recorded; it is noted that in some cases significant solvent effects on the SCO thermodynamics have been reported.[5] SCO is inherently a molecular property, which can be traced to a balance of competing enthalpic and entropic contributions. The weakened iron-donor bonds in the HS state render both the SCO enthalpy and the entropy positive, $\Delta_{SCO}H > 0$ and $\Delta_{SCO}S > 0$. Since both quantities largely reflect the peculiarities of metal-ligand bonding, targeted tuning of the SCO thermodynamics through ligand design appears to be straightforward. In terms of ligand-field theory, for instance, *strong-field ligands* from the upper end of the spectrochemical series are predicted to support large splitting among the non-bonding t_{2g} set and the anti-bonding e_g* set. It is common sense, that the stabilization of LS iron(II) complexes largely derives from mixing of metal-borne t_{2g} orbitals with potent acceptor states of the ligand with π* symmetry. Accordingly, solution data has been used for the construction of structure-property relationships within several ligand families that can be taken as a test of this hypothesis.[6–8] These studies have led to a more differentiated view of what actually is meant with the terminus *strong ligand field*. Halcrow and Deeth's blended experiment-theory scan across the bpp ligand family (bpp = 2,6-di{pyrazol-1-yl}pyridine) revealed opposing effects on SCO thermodynamics of terminal pyrazol and central pyridine substitution, consistent with differential resonance stabilization. On the other hand, Jakubikova's exhaustive DFT study on 2,2′-bipy derivatives somewhat surprisingly identified the ligands' action as a π-donor to be as important as their established role as π-acceptors. These studies exemplarily show that the molecular factors of SCO are not yet fully understood. Clearly the extension of molecular SCO studies to include further ligand families is in place.

In this work we study the variation of SCO behavior across a series of eight iron(II) complexes [Fe**X**(py)$_2$] deriving through backbone substitution from a common planar directing $N_2O_2^{2-}$ ligand of the Jäger type (Scheme 1). Keeping constant the *o*-phenylenediamine bridge and axial ligation through two pyridine molecules, the effects of substitution in the *meso*- and *O*-terminal positions of the equatorial plane could be studied in isolation. Magnetic response is recorded both in the solid state (SQUID magnetometry) and in solution (^{1}H NMR spectroscopy). The recorded thermodynamic data are discussed in terms of molecular structure and electronic effects, addressed through X-ray crystallography and extended DFT modelling.

Results and Discussion

Synthesis and characterization of iron(II) complexes

The syntheses of the ligands H$_2$**1**–H$_2$**4** and their bis(pyridine) iron(II) complexes were published previously; reviewed by Weber and Jäger.[9,10] The proto-ligands H$_2$**5**–H$_2$**8** were synthesized in good yields from *o*-phenylenediamine and the respective keto-enol ethers, as summarized in Scheme 1.[3,11–13] The ^{1}H NMR resonance pattern of the proto-ligands is in agreement with a predominant formulation as the keto-enamine tautomer.[13] It is noted that the complementary *salophen* ligand family rather justifies an enol-imine description. The desired complexes were obtained in a one-pot synthesis where the proto-ligand was agitated with iron(II) acetate in a mixture of methanol and pyridine to yield complexes [Fe(**5**–**8**)(py)$_2$] in a single step. It is also possible to heat the corresponding methanol precursor complexes [Fe(**5**–**8**)(MeOH)$_2$] in pyridine and then precipitate the desired pyridine complexes with water.

In both scenarios the products were isolated from their pyridine solutions as intensely colored powders either through crystallization or through precipitation with excess water. Elemental analysis is in agreement with the expected stoichiometry. In some cases, additional pyridine or water molecules co-crystallized as could be supported by X-ray crystallography (see below). While solutions of [Fe**5**–**7**(py)$_2$] were highly sensitive toward the presence of oxygen, solid samples were less susceptible. [Fe**8**(py)$_2$] with $R^1 = CF_3$ was clearly more inert towards oxygen also in solution. SQUID magnetometry revealed these solid powders to be paramagnetic at room temperature with effective magnetic moments being in agreement with HS iron(II) centers (more details below). IR spectra obtained of the powdered samples reveal the expected trends (Figure 1). In particular, complexes with non-coordinating carbonyl moieties ($R^2 = CO_2Me$; CO_2Et; COPh) feature prominently around 1700 cm^{-1}, typical of the intense ν(C=O) valence mode. Consequently, this spectral region is silent for compounds lacking free carbonyls; [Fe**4**(py)$_2$] with $R^2 = CN$, for instance,

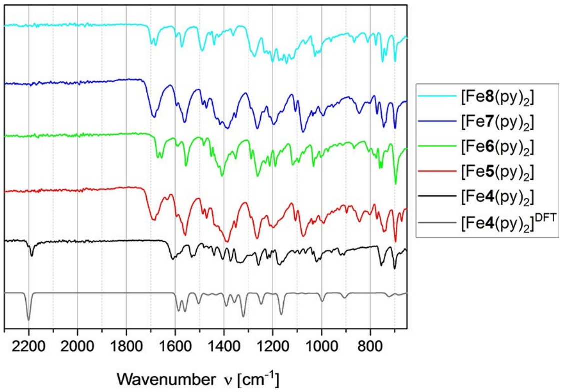

Figure 1. Vibrational spectra of powdered samples of [Fe**4**(py)$_2$] to [Fe**8**(py)$_2$] (ATR crystal; room temperature); for sake of comparison, a DFT-derived spectrum of HS-[Fe**4**(py)$_2$] is shown (grey line).

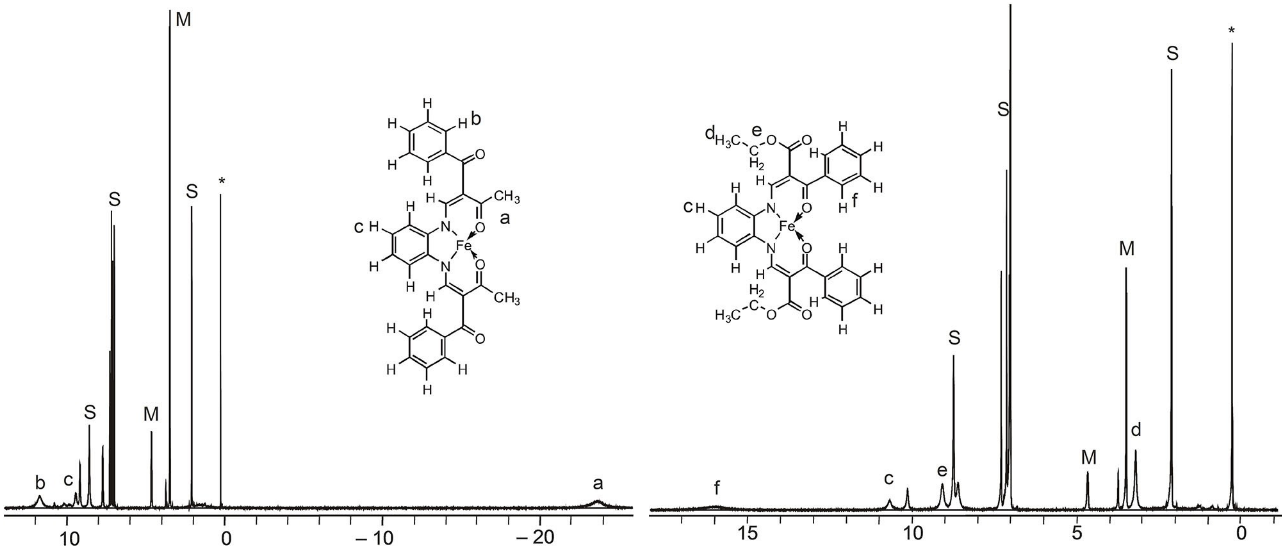

Figure 2. ^{1}H NMR spectra recorded of [Fe**5**(py)$_2$] (left) and [Fe**6**(py)$_2$] (right) in a mixture of pyridine-d_5 and toluene-d_8 (1:1) at $T = 328$ K (55 °C, 400 MHz); signal assignment based on chemical shift and signal width; S denotes residual solvent signals pyridine and toluene, M denotes to methanol from the precursor complex and * to an unknown contamination of the NMR solvent.

exhibits an intense resonance at 2200 cm^{-1} instead, diagnostic of a nitrile moiety. The overall appearance and the intensity pattern of the IR spectrum of [Fe**4**(py)$_2$] is well captured by a DFT-derived spectrum (grey in Figure 1).

Strongly broadened ^{1}H NMR spectra of [Fe**5**/**6**(py)$_2$] likewise support formulations as the HS species in all cases. Exemplary spectra recorded in a mixture of pyridine-d_5 and toluene-d_8 (1:1) at 55 °C are shown in Figure 2. In both cases, the expected number of resonances could be identified and assigned, based on chemical shift arguments, signal width and a comparison with the previously published complexes. Of particular diagnostic value is a broad resonance of [Fe**5**(py)$_2$] at very high field, namely at −25 ppm (a). Similar observations have been made by Weber and Walker with [Fe**1**(py)$_2$] and [Fe**2**(py)$_2$].[14] The latter two complexes showed high-field resonances around $\delta = -25$ ppm as they likewise share the substituent R^1=Me adjacent to the coordinated carbonyl moiety. In keeping with this assignment, high-field signals are absent for [Fe**6**(py)$_2$] with R^1=Ph and they were absent also for [Fe**3**(py)$_2$] with R^1=CO$_2$Et.[14]

With all other resonances being unexceptional, the juxtaposition of the phenyl-ring close to the iron(II) center in [Fe**6**(py)$_2$] (f) results in substantial down-field shift of the phenyl-borne *ortho*-H resonances to $\delta = 16$ ppm.

Solid-state structures

Crystals suitable for X-ray structure analysis of [Fe**6**(py)$_2$] were obtained by recrystallization of the isolated powders from mixtures of methanol and pyridine. For [Fe**7**(py)$_2$] crystals suitable for X-ray structure analysis were obtained from the filtrate. The crystallographic data for [Fe**6**(py)$_2$] were obtained at 173 K. [Fe**7**(py)$_2$] was studied at two different temperatures (170 K and 220 K) that frame the first spin transition in SQUID data (see below). The crystallographic data are summarized in Table S1. [Fe**6**(py)$_2$] crystallizes in the monoclinic space group $P2_1/n$ with the asymmetric unit containing two complex units and two additional pyridine molecules, giving rather [Fe**6**(py)$_2$]×py. Due to the strong disorder of the co-crystallized pyridine molecule, only a structural motif can be discussed. The asymmetric unit with the atom numbering scheme is displayed in Figure 3. The co-crystallized pyridine molecules are, as mentioned before, strongly disordered at $T = 173$ K. Selected bond lengths and angles within the inner coordination sphere are summarized in Table 1. At the measured temperature the

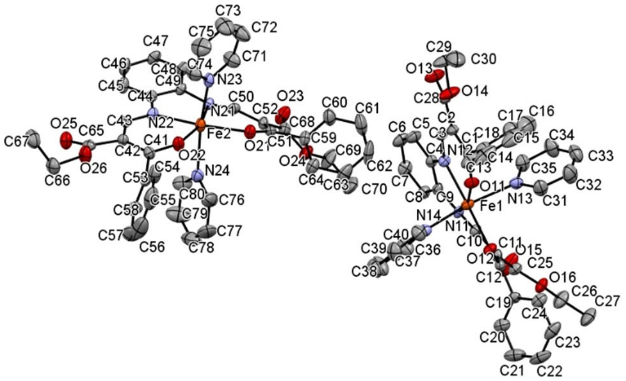

Figure 3. ORTEP drawing of the asymmetric unit of the motif of [Fe**6**(py)$_2$] × py (174 K) with the atom numbering scheme used. Co-crystallized solvent molecules and hydrogen atoms are omitted for clarity. Thermal ellipsoids are presented at 50 % level. (For further drawings see Figure S1 and S2.)

Table 1. Selected bond lengths (Å) and angles (°) within the inner coordination sphere of the iron(II) complexes [Fe**6**(py)$_2$] × py and [Fe**7**(py)$_2$] at various temperatures.

		T [K]	Fe–N$_{eq}$	Fe–O$_{eq}$	Fe–N$_{ax}$	O$_{eq}$–Fe–O$_{eq}$	N$_{ax}$–Fe–N$_{ax}$
[Fe**6**(py)$_2$]×py	Fe1	173	2.118(3), 2.128(3)	2.042(2), 2.076(2)	2.241(3), 2.213(3)	113.93(9)	167.13(11)
	Fe2		2.101(3), 2.132(3)	2.071(2), 2.034(2)	2.196(3), 2.247(3)	112.80(9)	168.07(11)
[Fe**7**(py)$_2$],	Fe1	170	1.886(4), 1.888(4)	1.941(3), 1.918(4)	1.984(5), 1.998(5)	88.89(15)	174.85(18)
	Fe2		2.087(4), 2.085(4)	2.004(4), 1.997(4)	2.241(4), 2.340(4)	108.00(16)	175.24(16)
[Fe**7**(py)$_2$],	Fe1	220	2.092(2), 2.0799(19)	2.0065(17), 2.0279(16)	2.287(2), 2.207(2)	109.21(7)	169.29(7)
	Fe2		2.089(2), 2.0846(19)	2.0002(19), 2.0136(18)	2.286(2), 2.256(2)	108.60(7)	176.11(8)

complex is clearly in the HS state considering the average Fe–N bond length and of 2.12 Å (eq)/2.22 Å (ax) and an O$_{eq}$–Fe–O$_{eq}$ angle of 113.93 and 112.80°.[9,10] Further details on the packing of the molecules in the crystal are given in the Supporting Information, Figure S2 and Table S2. By contrast, [Fe**7**(py)$_2$] crystallizes solvent-free in the triclinic system, exhibiting two complex molecules in the asymmetric unit. The asymmetric unit with the atom numbering scheme for both temperatures is displayed in Figure 4. Notably, the cell parameters obtained of [Fe**7**(py)$_2$] significantly differ at $T = 170$ K and $T = 220$ K. In keeping with the sharply decreased crystal quality at the lower temperature, extensive molecular and supramolecular rearrangements can be suspected. Indeed, the high-temperature structure reveals two HS-configured complexes, with an average Fe–N bond length of 2.08 Å (eq) and 2.26 Å (ax). By contrast in the low-temperature structure one of the molecules (Fe$_1$) is found in the LS state.

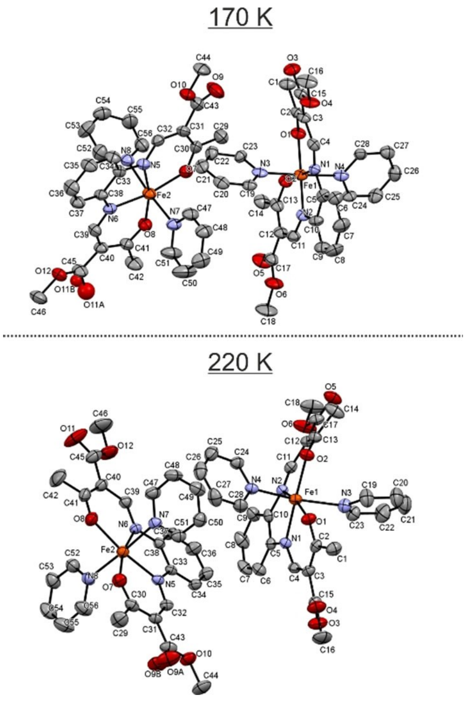

Figure 4. ORTEP drawing of the asymmetric units of crystal structures of [Fe**7**(py)$_2$] obtained at $T = 170$ K (left) and at $T = 220$ K (right) with the used atom numbering scheme. Thermal ellipsoids are presented at 50% level. Hydrogen atoms are omitted for clarity.

The average Fe–N bond lengths of 1.89 Å (eq) and 1.99 Å (ax) in the Fe$_1$-containing unit of [Fe**7**(py)$_2$] are clearly in a range typical for iron(II) in the LS state whereas all values of the inner coordination sphere around Fe$_2$ indicate conserved HS character.[9,10] At both temperatures disorder of the ester group can be observed, which is not unusual for this kind of compound. The packing of the molecules in the crystal and details on the intermolecular interactions are given in the Supporting Information, Figure S3 and Tables S3 and S4. Combined with the previously reported crystal structures of [Fe**1**(py)$_2$] to [Fe**4**(py)$_2$],[9,15,16] we can establish a broad inquiry in the effects of equatorial substitution on the coordination metrics. Therein we cover nine (predominantly) HS structures and three (predominantly) LS structures as can be concluded from pertinent metrical data summarized in Tables 1 and 2. While poor crystal quality so far interfered with structure analysis of [Fe**8**(py)$_2$], it is noted that the molecular structure of its coordination polymer with 4,4'-bipyridine, {[Fe**8**(bipy)]}$_n$, could be recently resolved.[3] The coordination metrics were fully in accord with the LS state structures assembled in Table 2.

The low-temperature structures obtained of [Fe**1**(py)$_2$] and [Fe**2**(py)$_2$] largely resemble molecule **b** obtained of [Fe**7**(py)$_2$] at $T = 170$ K with respect to the coordination metrics. Diagnostic markers of a low spin configured iron(II) center are both short equatorial (d(Fe-O$_{eq}$) and d(Fe-N$_{eq}$) < 1.96 Å) and axial bond lengths (d(Fe-N$_{ax}$) < 2.03 Å). Such short iron-donor distances are possible only with a $t_{2g}{}^6e_g{}^0$ configuration. As a secondary marker, the opening angle O$_{eq}$-Fe-O$_{eq}$ is close to 90°, indicating

Table 2. Coordination metrics of crystal structures in the substitution series [Fe**1**(py)$_2$] to [Fe**4**(py)$_2$].

	[Fe**1**(py)$_2$]^a	[Fe**2**(py)$_2$]^b	[Fe**3**(py)$_2$]^a	[Fe**4**(py)$_2$]^c
	LT/HT	**LT/HT**	**LT**	**LT**
Fe–O	1.955/2.017	1.930/2.009	2.046	2.050
Fe–O'	1.962/1.990	1.948/1.992	2.048	2.083
Fe–N$_{eq}$	1.918/2.053	1.894/2.061	2.109	2.100
Fe–N$_{eq}$'	1.923/2.062	1.906/2.074	2.102	2.141
Fe–N$_{ax}$	2.023/2.195	2.007/2.226	2.239	2.246
Fe–N$_{ax}$'	2.025/2.256	2.025/2.269	2.262	2.262
O–Fe–O'	92.4/106.3	90.0/107.3	112.0	108.0
N$_{ax}$–Fe–N$_{ax}$'	–	176.1/175.6	–	170.3
	SCO	**SCO**	**HS**	**HS**

a: taken from Ref. [9]; **b**: taken from Ref. [15]; **c** taken from Ref. [16].

a largely undisturbed octahedral coordination. By contrast, massively expanded bond lengths by ≈ 10 pm (d(Fe-O$_{eq}$)) and > 20 pm (d(Fe-N$_{eq}$) and d(Fe-N$_{ax}$)) prevail in the high-temperature structures of [Fe**1**(py)$_2$], [Fe**2**(py)$_2$] and [Fe**7**(py)$_2$]. Equatorial bond expansion translates into an increased opening of O$_{eq}$-Fe-O$_{eq}$ > 110°. [Fe**1**(py)$_2$], [Fe**2**(py)$_2$] and [Fe**7**(py)$_2$] at high temperature therefore share the temperature-invariant metrics of [Fe**3**(py)$_2$], [Fe**4**(py)$_2$] and [Fe**6**(py)$_2$] and can be readily identified to be likewise in the $t_{2g}{}^4e_g{}^2$ HS configuration with populated anti-bonding orbitals. These observations could be fully corroborated by magnetic measurements of powdered samples.

SQUID magnetometry

Previous work had shown that all members of the series [Fe**X**(py)$_2$] with **X** = **1**–**4**, were entirely in the HS state at room temperature.[10] While the HS character of [Fe**3**(py)$_2$] and [Fe**4**(py)$_2$] was conserved even at lowest temperatures, [Fe**1**(py)$_2$] and [Fe**2**(py)$_2$] underwent complete SCO in the solid state upon cooling with $T_{1/2}$ = 220 K (gradual) and 190 K (narrow hysteresis), respectively. The extension of our inquiry in the magnetic behavior to the new members of the series with **X** = **5**–**8** led to further diversification of the SCO phenomenology, illustrated in Figure 5. Firstly, [Fe**5**(py)$_2$] undergoes an abrupt SCO at $T_{1/2}$ = 105 K, giving rise to a narrow hysteresis with a width of 2 K. By contrast, [Fe**6**(py)$_2$] shows a rather gradual SCO, centered at $T_{1/2}$ = 200 K. The gradual transition in the bulk material is most probably due to the bulky phenyl rings. Please note that the single crystals with the composition [Fe**6**(py)$_2$] × py remain in the HS state across the entire temperature range, as shown in the Supporting Information, Figure S4. Solution-phase NMR studies later confirmed SCO also for isolated molecules of [Fe**5**(py)$_2$] and [Fe**6**(py)$_2$]. Remarkable is the complex behavior of [Fe**7**(py)$_2$], the structure of which differs only marginally from parent [Fe**1**(py)$_2$] in the nature of the substituent R^2; that is, R^2 = CO$_2$Et and CO$_2$Me for [Fe**1**(py)$_2$] and [Fe**7**(py)$_2$], respectively. As is shown in Figure 5, this slight difference in remote substitution translates into markedly different magnetic response. [Fe**7**(py)$_2$] reveals a step-wise SCO, with the steps being centered at $T_{1/2}$ = 217 K and 110 K. Notably, both steps are abrupt and give rise to hysteretic splitting of the rising and falling branches by 16 K and 9 K, respectively. With a view to the aforementioned results from X-ray crystallography we attribute the first step to complete SCO of one out of two iron(II) sites in the crystal lattice (see above). Finally, [Fe**8**(py)$_2$] with carbonyl adjacent CF$_3$-groups undergoes complete and abrupt SCO with $T_{1/2}$ = 175 K and shows a narrow, 3 K wide hysteresis. In summary, at sufficiently low temperature, the substitution series [Fe**X**(py)$_2$] allows for complete SCO in the solid state in six out of eight cases; only [Fe**3**(py)$_2$] and [Fe**4**(py)$_2$] remain in the HS state across the entire temperature range. VT-NMR spectroscopy was therefore used to address the question whether or not the HS character is a molecular property of the latter two compounds.

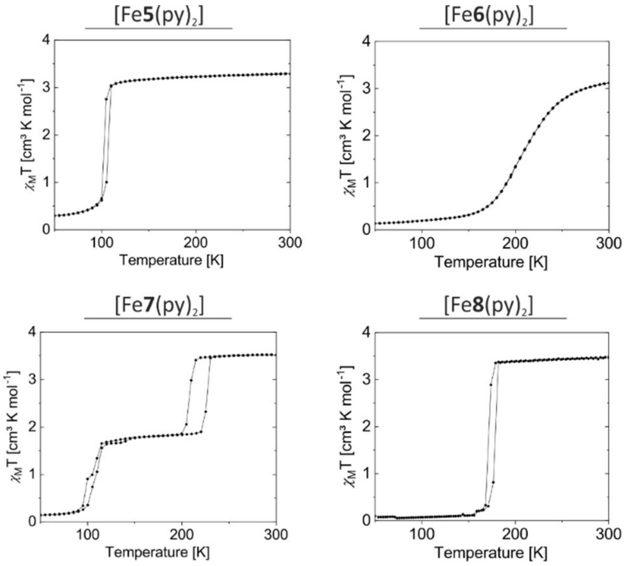

Figure 5. Plots of the $\chi_M T$ product vs. Temperature in the range 300–50–300 K (scan rate 5 K/min; H = 5000 Oe).

VT-NMR spectroscopy

Previous studies had observed that NMR spectra of [Fe**3**(py)$_2$] with R^1 = R^2 = CO$_2$Et undergo continuous evolution upon cooling which is fully in agreement with Curie behavior of an enduring paramagnet down to T = 180 K. On the other hand, chemical shifts recorded for [Fe**1**(py)$_2$] and [Fe**2**(py)$_2$] strongly deviated from the linear 1/T dependence implied by Curie's law.[14] These deviations rather signaled spin-pairing to partially form the LS state, a notion which was supported by Evans NMR. Deviations of NMR parameters from Curie's law have been associated with SCO in several previous cases.[17] Clearly, the nature of substituents R^1 and R^2 serves to significantly modulate the SCO energies. This notion is underpinned by the results in the present study obtained in VT-NMR scans of [Fe**5**(py)$_2$] and [Fe**6**(py)$_2$] in toluene/pyridine mixtures. An exemplary Curie plot of the temperature dependence of chemical shifts for various proton sites in [Fe**6**(py)$_2$] is shown in Figure 6, the corresponding results for [Fe**5**(py)$_2$] and all further details for the determination of the HS fraction γ_{HS} are given in the Supporting Information, Figure S5. Between 370 K > T > 270 K the plots are approximately linear, but tend to massively deviate from linearity at even lower temperature. From the recorded chemical shifts, δ_{obs}, γ_{HS} was calculated as discussed in the SI according to equation 1.

$$\delta_{obs} = \gamma_{HS} \times \delta_{HS}\ (T) + (1 - \gamma_{HS}) \times \delta_{LS} \tag{1}$$

Therein the chemical shifts for the LS species δ_{LS} were taken as invariant with temperature and equal to the chemical shift of the free ligand, whereas the temperature dependence of the HS chemical shifts δ_{HS} (T) were extrapolated along Curie's law from the linear branch of the high-temperature data.

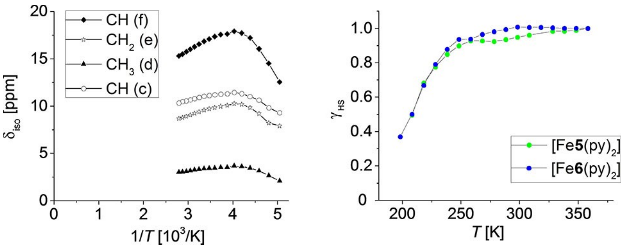

Figure 6. (left) Curie plot of ^1H NMR chemical shifts recorded of [Fe**6**(py)$_2$] in a mixture of pyridine-d_5 and toluene-d_8 (1:1) in the temperature range between 200 K and 360 K (400 MHz); (right) averaged HS fractions of [Fe**5**(py)$_2$] and [Fe**6**(py)$_2$]. Computed from chemical shift data according to equ. 1. The complete data for both complexes are given in the Supporting Information, Figure S5.

The resulting computed HS fractions are given in the SI, Figure S5, for both complexes. Upon decrease of temperature, the HS fraction massively decreases, reaching fractions of $\gamma_{HS} \approx 0.4$ at the lowest available temperature of 200 K. $T_{1/2}$ where $\gamma_{HS} = \gamma_{LS}$ can be estimated to be around 205 K (Figure 6, right). It should be compared with the locked-HS state of the single crystals of [Fe**6**(py)$_2$] × py. Interestingly, a very similar plot of $\gamma_{HS}(T)$ prevails for [Fe**5**(py)$_2$], indicating an only marginal difference in SCO thermodynamics of both complexes. This notion is corroborated by Van't Hoff analysis of the entire temperature scans of $\gamma_{HS}(T)$. The corresponding thermodynamic parameters, $\Delta_{SCO}H$ and $\Delta_{SCO}S$, are summarized in Table 3. For the sake of comparison, the data of [Fe**1**(py)$_2$] and [Fe**2**(py)$_2$] are re-plotted from Ref.[14] It is noted that, due to the incomplete coverage of the sigmoidal curves, the extracted enthalpy and entropy carry a significant uncertainty. Suffice to say here, that there is only minor scatter among the thermodynamics of the complexes [Fe**1**(py)$_2$], [Fe**2**(py)$_2$], [Fe**5**(py)$_2$] and [Fe**6**(py)$_2$], pointing to a likewise minor influence of the substituents R^1 and R^2 on the SCO. By contrast, the tendency of [Fe**3**(py)$_2$], [Fe**4**(py)$_2$] not to undergo SCO in solution (and in the solid) indicates disfavored thermodynamics. The largely conserved molecular structure across the entire series of complexes renders large fluctuations in SCO entropy unlikely. Therefore, the influence of the substitution pattern on the enthalpic factors of SCO was studied through DFT methods.

Table 3. Thermodynamic parameters of solution phase SCO as obtained from ^1H NMR temperature scans.

	[Fe**1**(py)$_2$]^a	[Fe**2**(py)$_2$]^a	[Fe**5**(py)$_2$]	[Fe**6**(py)$_2$]
$\Delta_{SCO}H$ [kJ mol^{-1}]	18.2	25.5	20.2	25.1
$\Delta_{SCO}S$ [J mol^{-1} K^{-1}]	88	121	98	121
$T_{1/2}$ [K]	207	211	206	207

^{a} taken from Ref. [Walker, Weber].

DFT structure optimization

The impact of remote substitution on the coordination metrics was addressed with DFT methods across the entire complex series given in Scheme 1; both the LS ($S=0$) and the HS state ($S=2$) were considered. Optimization with the BP86 functional and large triple-ζ basis sets was calibrated against experimental metrics whenever accessible (for Computational Details, see the Experimental Section). Harmonic frequencies were computed for the HS states of all complexes; the absence of imaginary modes identified the minima as stationary points on the energy hypersurface (a computed IR spectrum of HS-[Fe**4**(py)$_2$] is shown in Fig. 1). Pertinent metrical data are summarized in Table 4. Comparison with the experimental data (Tables 1 and 2; see above) reveals an excellent match with respect to metal-ligand bond lengths and core angles.

As was apparent from the experimental data in Tables 1–2 also, the N_2O_2 planar platform largely predefines the coordination metrics, both in the HS and the LS form. In particular, the bond lengths of the enaminate nitrogen atoms very narrowly cluster at 1.90 ± 0.01 Å and 2.08 ± 0.01 Å in the LS and HS states, respectively.

These values closely match the experimental data. More diversity prevails in the Fe-O_{eq} bond lengths, likely due to the enhanced flexibility of the open end of the binding pocket. Here we find two clusters of values, both in the HS and the LS state. On the one hand, values of 1.94 ± 0.01 Å and 2.01 ± 0.01 Å in the LS and HS states, respectively, cover the majority of the complex series. It is only for [Fe**3**(py)$_2$] and [Fe**4**(py)$_2$] on the other hand that we find the Fe-O_{eq} bonds consistently expanded by 4–5 pm, irrespective of the spin state. It is noted,

Table 4. Coordination metrics of DFT-optimized structures of the substitution series [Fe**1**(py)$_2$] to [Fe**8**(py)$_2$] for $S=0$ (LS) and $S=2$ (HS); italicized data correspond to structures for which comparison is possible with experimental data in Tables 1–2.

	[Fe**1**(py)$_2$]		[Fe**2**(py)$_2$]		[Fe**3**(py)$_2$]		[Fe**4**(py)$_2$]		[Fe**5**(py)$_2$]		[Fe**6**(py)$_2$]		[Fe**7**(py)$_2$]		[Fe**8**(py)$_2$]	
	LS	HS	LS	HS	LS	HS	LS	HS	LS	HS	LS	HS	LS	HS	LS	HS
Fe–O	1.937	2.013	1.937	2.011	1.966	2.053	1.973	2.065	1.933	2.004	1.936	2.014	1.939	2.014	1.935	2.015
	1.938	2.011	1.934	2.020	1.959	2.055	1.973	2.067	1.944	2.022	1.936	2.014	1.937	2.011	1.933	2.022
Fe–N_{eq}	1.893	2.080	1.892	2.076	1.895	2.085	1.903	2.089	1.891	2.077	1.902	2.084	1.893	2.079	1.897	2.077
	1.893	2.078	1.892	2.083	1.898	2.086	1.902	2.090	1.894	2.080	1.902	2.087	1.893	2.078	1.897	2.079
Fe–N_{ax}	1.950	2.171	1.953	2.170	1.949	2.153	1.954	2.153	1.955	2.174	1.949	2.177	1.951	2.171	1.959	2.178
	1.982	2.260	1.982	2.253	1.968	2.243	1.970	2.238	1.977	2.290	1.984	2.247	1.982	2.260	1.990	2.238
O–Fe–O	87.1	110.5	87.4	111.5	87.4	109.7	85.9	107.4	87.1	109.3	86.2	109.2	87.1	110.6	86.8	109.9
N_{ax}–Fe–N_{ax}	178.2	178.3	178.2	178.0	177.8	176.8	177.8	176.4	178.3	178.6	178.1	177.7	178.3	178.3	178.1	177.3

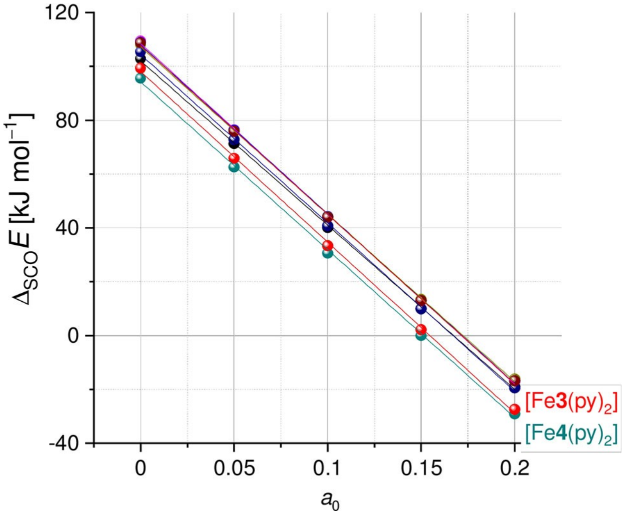

Figure 7. DFT-derived (B3LYP–D/TZVP) apparent SCO energies of complexes [Fe**X**(py)$_2$] as a function of the amount of exact Fock-exchange a_0.

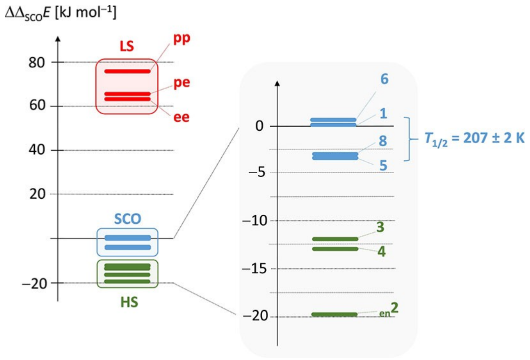

Figure 8. Relative SCO energies $\Delta\Delta_{SCO}E$ of the substitution series [Fe**X**(py)$_2$] (**X** = **1**, **2**..., **8**); energies are given relative to [Fe**2**(py)$_2$]; additional data of the ethylenediamine-derived system [Fe$_{\mathbf{en}}$**2**(py)$_2$] and of macrocyclic systems **pp**, **pe**, and **ee** featuring **p**henylenediamine and **e**thylenediamine bridges; colors denote the experimentally observed SCO behavior.

that this feature is apparent in the experimental data of [Fe**3**(py)$_2$] and [Fe**4**(py)$_2$] also. Notably, these two outliers are temperature-invariant HS complexes, both in the crystal and in solution. This coincidence indicates a molecular origin of the HS preference, which must be associated with the nature of the substituent, R^1 = OEt.

Computation of SCO energies

The impact of the substitution pattern on the SCO energies was addressed with DFT methods. Improved precision was obtained through a Fock-exchange scan via variation of the exact exchange a_0 in the B3LYP functional. Linear plots of the derived apparent SCO energies against a_0 show slopes that reflect the extent of SCO-related metrical changes (equ. 2).[18,19] That is, the slopes of the plots will be structure-independent, if belonging to the same family of complexes. By contrast, the offset of the plots will reflect the structure-bias of the SCO energies. The resulting plots are shown in Figure 7, the results of the linear regression can be found in Table 5.

$$\Delta_{SCO}E = \Delta_{SCO}E^0 + (\delta_{SCO}E \times a_0) \qquad (2)$$

The common slope of the linear fits largely supports the notion of [Fe**X**(py)$_2$] being a family of complexes. It is only [Fe**8**(py)$_2$] where the slope is significantly smaller, indicating electronically slightly deviant behavior. More instructive is the vertical ordering of the lines. While most lines (almost) coincide, the apparent SCO energies of [Fe**3**(py)$_2$] and [Fe**4**(py)$_2$] are significantly smaller across the entire Fock-exchange scan by > 10 kJ mol^{-1}. With a view to the limited accuracy of computed absolute SCO energies $\Delta_{SCO}E$, we go on with discussion being based on relative SCO energies $\Delta\Delta_{SCO}E$. The latter measure the deviation from a pre-selected standard complex, in the following $\Delta\Delta_{SCO}E = \Delta_{SCO}E - \Delta_{SCO}E(\text{ref})$ (with ref = [Fe**2**(py)$_2$]; $T_{1/2}$ = 211 K; $\Delta_{SCO}S$ = 121 J K^{-1} mol^{-1}; $\Delta_{SCO}H$ = 25.5 kJ mol^{-1}; Table 3). Internal referencing within the complex family gives most effective cancellation of DFT-inherent systematic errors, as has been shown previously.[17,20] The averaged values of the relative SCO energies are shown in Figure 8 (standard error ≤ 1.5 kJ mol^{-1}). Added to the plot is a number of related systems.

For instance, in [Fe$_{\mathbf{en}}$**2**(py)$_2$] the phenylene bridge of [Fe**2**(py)$_2$] is replaced by ethylene, whereas **pp**, **pe**, and **ee** denote macrocyclic ligands with an N_4^{2-} donor set and a substitution pattern deriving from **2**. In experimental studies [Fe$_{\mathbf{en}}$**2**(py)$_2$] had been identified as a HS system,[9] whereas the macrocyclic complexes **pp**, **pe**, and **ee** preferred the LS state.[21] Structure plots of these systems are given in Figure S6, SI. The computed relative SCO energies give an energy ladder spanning a range of ca. 100 kJ mol^{-1}, with [Fe**2**(py)$_2$] defining zero energy. The energy ordering found with DFT gives three separate regimes. Firstly, according to DFT, the three macrocycles possess strongly favored LS states. Relative energies exceed $\Delta\Delta_{SCO}E$ > 60 kJ mol^{-1}

Table 5. Fitting results of the linear regressions for complexes [Fe**X**(py)$_2$] in Scheme 1; energies in kJ mol^{-1}.

X =	1	2	3	4	5	6	7	8
$\delta_{SCO}E$	−629(7)	−633(7)	−635(9)	−624(9)	−626(8)	−622(6)	−628(7)	−610(6)
$\Delta_{SCO}E^0$	108(1)	108(1)	98(1)	94(1)	104(1)	107(1)	108(1)	102(1)
R^2	0.9995	0.9995	0.9992	0.9992	0.9994	0.9996	0.9995	0.9996

in all cases. If a common entropy $\Delta_{SCO}S = 100\ \mathrm{J\,K^{-1}\,mol^{-1}}$ is assumed for all complexes, the SCO energies translate into transition temperatures well beyond $T_{1/2} = 800$ K for **ee**, **pe** and **pp**. The lower end of the energy ladder constitutes of the ethylenediamine-derived complex [Fe$_{\mathbf{en}}$**2**(py)$_2$] and the previously discussed complexes [Fe**3**(py)$_2$] and [Fe**4**(py)$_2$], both equipped with $R^1 = OEt$. The three complexes reside at $\Delta\Delta_{SCO}E < -10\ \mathrm{kJ\,mol^{-1}}$ translating into molecular transition temperatures below $T_{1/2} = 100$ K. In both cases discussed, therefore the computed energies fully match the experimental phenomenology symbolized by the colors; that is, red for LS and green for HS. Finally, the remaining members of the family narrowly crowd around $\Delta\Delta_{SCO}E \approx 0\ \mathrm{kJ\,mol^{-1}}$, with a maximum deviation of $-3\ \mathrm{kJ\,mol^{-1}}$ (blue in Figure 8). Computation thus suggests narrowly crowding transition temperatures also, with $\Delta T_{1/2} < 30$ K, relative to [Fe**2**(py)$_2$]. A very similar range of SCO energies has been recently reported by us for a number of π-extended congeners of [Fe**7**(py)$_2$], indicating an only minor role of π-modulation.[22] Comparison with the NMR-derived experimental transition temperatures of $T_{1/2} = 207 \pm 2$ K emphasizes the highly satisfying quality of the prediction.

Conclusion

In the period following the landmark reviews collected by Gütlich and Goodwin in 2004,[23] spin crossover research took a clear conceptual realignment towards application. That is, material science with a focus on device-design makes up the vast majority of spin crossover studies. As an inevitable side-effect of this development which emphasizes solid materials, the inherent *molecule character* of the phenomenon is biased and often overridden by packing effects. Structure-function relationships therefore are a blend of molecular and supramolecular properties. It has been only very recently that the molecular factors defining and modulating the energy spacing among spin states have been rigorously addressed in concerted theory-experiment efforts; the reader is reminded of the insightful studies by, among others, Deeth and Halcrow *et al.* that made use of spectroscopic studies of isolated actors supplemented by DFT computation.[6] While this approach allowed for some surprising turns, to date only a limited number of complex families has been addressed in such detail.

In this work we moved the focus to a family of octahedral iron(II) complexes of planar-directing Schiff-base like ligands of the Jäger type with invariant axial ligation and invariant *o*-phenylene bridge. Accompanied by a DFT inquiry in the SCO energetics and structural changes, eight members of the family were addressed experimentally in the solid state (X-ray diffraction and SQUID magnetometry) and in solution (VT-NMR spectroscopy). The theoretical section additionally covered topological mutants with an ethylene bridge (en) or a number of macrocyclic N_4^{2-} ligands. As a matter of fact, the HS character of the en-derivative and the LS character of the macrocycle-derived systems, apparent from experiment, is likewise matched by DFT computed SCO energy. These extreme cases may be taken to define the Jäger-system overall variability in SCO energy that amounts to $\Delta\Delta_{SCO}E \approx 100\ \mathrm{kJ\,mol^{-1}}$.

Admittedly, the energy span of [Fe**X**(py)$_2$], directly addressable through remote ligand substitution, is much smaller at present, amounting to ca. 15 kJ mol^{-1}. This value should be compared with the related energy span of ca. 20 kJ mol^{-1} and ca. 25 kJ mol^{-1} computed by Deeth and Halcrow *et al.* and Jakubikova *et al.* for derivatives of 2,6-di{pyrazol-1-yl}pyridine and 2,2′-bipyridine, respectively.[6,7] With a view to the narrow energy span in [Fe**X**(py)$_2$], it is highly motivating to note that our DFT routines were able to correctly assign the solution SCO behavior across the entire substitution series. Through this we could further specify the origin of enduring HS character of a group of complexes in the solid-state. Molecule-inherent HS complexes which reflect a diminished ligand-field can be safely differentiated from supra-molecularly-trapped HS complexes.

Experimental Section

Synthesis

Iron(II) acetate,[24] [Fe**5**(MeOH)$_2$]/H$_2$**5**,[11] H$_2$**6**,[12] H$_2$**7**[13] and H$_2$**8**[3] were synthesized as described in literature. Methanol was purified as described in literature. Pyridine was purchased from Acros organics (99.5 %, extra dry over molecular sieve, nitrogen flushed) and used as supplied. All air sensitive syntheses were carried out under argon 5.0 using Schlenk tube techniques.

X-ray Structure Analysis

The intensity data of [Fe**6**(py)$_2$] were collected with an Oxford XCalibur diffractometer using graphite-monochromated $Mo_{K\alpha}$ radiation. The data was corrected for Lorentz and polarization effects. The structures were solved by direct methods using SIR97[25] and refined by full-matrix least-square techniques against F_0^2 (SHELXL-97).[26] The hydrogen atoms were included at calculated positions with fixed displacement parameters. All non-hydrogen atoms were refined anisotropically. The intensity data of [Fe**7**(py)$_2$] were collected with a Stoe StadiVari diffractometer using graphite-monochromated Mo-K_α radiation at 220 K and 170 K. The data were corrected for Lorentz and polarization effects. The structures were solved by direct methods (SIR-2019)[27] and refined by full-matrix least-square techniques against F_o^2-F_c^2 (SHELXL-2018).[28] All hydrogen atoms were calculated in idealized positions with fixed displacement parameters. ORTEP-III[29] was used for the structure representation and Mercury 2020.1[30] for the representation of the molecule packing.

Magnetic measurements on the bulk materials were carried out using a SQUID MPMS-XL5 from Quantum Design with an applied field of 5000 G in the temperature range from 300 to 50 K in the settle mode. The samples were prepared in a gelatin capsule and held in a plastic straw. The raw data were corrected for the diamagnetic part of the sample holder and the diamagnetism of the organic ligand using tabulated Pascal's constants.[31]

IR spectra were recorded with a 520 FT-IR (NICOLET). Mass spectra were recorded with a Finnigan MAT 8500 with a data system MASPEC II. For CHN analysis a Unicube (ELEMENTAR) was used.

T-dependent NMR Spectroscopy: Pyridine-d_5 (D, 99,5 %) and toluene-d_8 (D, 99.6 %) were purchased from Euriso-top. The solvents were degassed with argon and stored over molecular sieves. The

NMR samples were prepared under argon by using Schlenk techniques and locally made sealing equipment. Saturated solutions of the iron(II) complexes were prepared in pyridine-d_5/toluene-d_8 (50/50 v/v) mixtures and stored in sealed or air-tight 5-mm NMR tubes. The NMR spectra were recorded on a JEOL EX 400e spectrometer operating at 400.182 MHz equipped with a variable-temperature unit over the temperature range −75 to +85 °C (198–358 K).

[Fe4(py)$_2$]

H_2**4** (0.5 g, 1.41 mmol, 1 eq.) and iron(II) acetate (0.39 g, 2.26 mmol, 1.6 eq) were dissolved in 11.4 mL pyridine (11.16 g, 141.1 mmol, 100 eq). 12 ml of MeOH were added and the mixture was heated to reflux for 1 h. After cooling to room temperature and storage at 8 °C for 24 h red-brown needles precipitated. The material was filtered off and washed two times with MeOH (2 mL). The precipitate was dried in vacuum. Yield: 0.37 g (566.40 g/mol, 46.3 %). Elemental analysis ($C_{28}H_{32}FeN_6O_4$, %) calcd: **C** 59.38 **H** 4.63 **N** 14.84; found: **C** 59.97 **H** 4.63 **N** 14.91. MS ((+)-DEI), 70 eV): m/z (%) 408 (100) [[Fe**4**]], 380 (35) $[C_{17}H_{18}FeN_3O_4]^+$, 352 (52) $[C_{14}H_8FeN_4O_4]$, 44 (84) $[C_2H_6N]^+$. **IR**: $\tilde{v}$ = 2982 (w, ν[–C–H]), 2188 (s, ν[–C≡N]), 1610 (s, ν[C=C]), 1532 (s, ν[C=C]).

{[Fe5(py)$_2$]·0.55 H$_2$O}

[Fe**5**(MeOH)$_2$] (0.3 g, 0.52 mmol, 1 eq.) was dissolved in pyridine (14.7 g, 185,8 mmol, 357 eq) and heated to reflux for 1 h. After cooling to room temperature 10 mL water were added. The reaction mixture was stored at −22 °C for 24 h. A fine brown crystalline solid precipitated. It was filtered, twice washed with methanol (2 mL) and dried in vacuum. Yield: 0.22 g (674.45 g/mol, 62.7 %). Elemental analysis ($C_{38}H_{32}FeN_4O_4 \cdot 0.55H_2O$, %) calcd: **C** 67.66 **H** 4.95 **N** 8.31; found: **C** 67.57 **H** 4.83 **N** 8.26. **MS** ((+)-DEI), 70 eV): m/z (%) 506 (98) [[Fe5]], 464 (62) $[C_{26}H_{20}FeN_2O_3]^{+\bullet}$, 105 (100) $[C_8H_9]^+$, 77 (98) $[C_6H_5]^+$, 43 (49) $[C_2H_3O]^+$. **IR**: $\tilde{v}$ = 3071 (w, ν[=C–H]), 2946 (w, ν[–C–H]), 2946 (w, ν[=C–H]), 1684 (m, ν[C=O]), 1559 (s, ν[C=C]).

[Fe6(py)$_2$]

H_2**6** (0.5 g, 0.97 mmol, 1 eq.) and iron(II) acetate (0.27 g, 1.56 mmol, 1.6 eq) were dissolved in pyridine (7.58 g, 97.5 mmol, 100 eq). 8 ml of MeOH were added and the mixture was heated to reflux for 1 h. After cooling to room temperature 5 mL of water were added. After storage at −22 °C for 24 h a red-brown fine crystalline powder precipitated. The material was filtered off and washed two times with MeOH (2 mL) and dried in vacuum. Yield: 0.25 g (724.60 g/mol, 35.6 %). Elemental analysis ($C_{40}H_{36}FeN_4O_6$, %) calcd: **C** 66.30 **H** 5.01 **N** 7.73; found: **C** 66.36 **H** 5.04 **N** 7.80. **MS** ((+)-DEI), 70 eV): m/z (%) 566 (62) [[Fe6]], 422 (31) $[C_{24}H_{18}FeN_2O_2]^{2+}$, 105 (88) $[C_8H_9]^+$7 (100) $[C_6H_5]^+$. **IR**: $\tilde{v}$ = 2976 (w, ν[CH_3]), 2923 (w, ν[CH_2]), 1671 (s, ν[C=O]), 1656 (s, ν[C=C]), 1557 (s, ν[C=C]).

Single crystals with the composition {[Fe**6**(py)$_2$] × py} were obtained from a pyridine solution after addition of water.

[Fe7(py)$_2$]

H_2**7** (0.5 g, 1.38 mmol, 1 eq.) and iron(II) acetate (0.38 g, 2.22 mmol, 1.6 eq) were dissolved in 10 mL pyridine (9.88 g, 124.8 mmol, 150 eq). 10 ml of MeOH were added and the mixture was heated to reflux for 1 h. After cooling to room temperature 7 mL water were added. After storage at −22 °C for 24 h brown needles crystallized from the reaction mixture. They were filtered, washed two times with methanol (2 mL) and dried in vacuum. Yield: 0.24 g(572.40 g/mol, 30.4 %) Elemental analysis ($C_{28}H_{28}FeN_4O_6$, %) calcd: **C** 58.75 **H** 4.93 **N** 9.79; found: **C** 58.66 **H** 4.79 **N** 9.85. **MS** ((+)-DEI), 70 eV): m/z (%) 414 (100) [[Fe7]], 383 (24) $[C_{17}H_{15}FeN_2O_5]^+$, 340 (40) $[C_{15}H_{12}FeN_2O_4]$, 309 (35) $[C_{14}H_9FeN_2O_3]$, 79 (38) $[C_5H_5N]$, 52 (45) $[C_4H_4]^{\bullet+}$, 44 (47) $[C_2H_4O]$. **IR**: $\tilde{v}$ = 3072 (w, ν[=C–H]), 2945 (w, ν[–C–H]), 1684 (s, ν[C=O]), 1562 (s, ν[C=C]).

[Fe8(py)$_2$]

H_2**8** (0.2 g, 0.40 mmol, 1 eq.) and iron(II) acetate (0.11 g, 0.64 mmol, 1.6 eq) were dissolved in 3.2 mL pyridine (3.21 g, 40.2 mmol, 100 eq). 10 ml of MeOH were added and the mixture was heated to reflux for 1 h. After cooling to room temperature 5 mL water were added. After storage at −22 °C for 24 h black needles crystallized from the mixture. They were filtered, twice washed with methanol (2 mL) and dried in vacuum. Yield: 0.18 g (708.40 g/mol, 63.2 %) Elemental analysis ($C_{30}H_{26}F_6FeN_4O_6$, %) calcd: **C** 50.87 **H** 3.70 **N** 7.91 found: **C** 51.00 **H** 3.82 **N** 7.93. **MS** ((+)-DEI), 70 eV): m/z (%) 550 (45) [[Fe8]], 408 (21) $[C_{16}H_{11}F_3FeN_2O_4]^{2+}$, 363 (42) $[C_{14}H_6F_3FeN_2O_3]^{3+}$, 79 (100) $[C_5H_5N]$, 52 (79) $[C_4H_4]^{\bullet+}$. **IR**: $\tilde{v}$ = 2987 (w, ν[CH_3]), 2919 (w, ν[CH_2]), 1698 (s, ν[C=O]), 1680 (s, ν[C=C]), 1573 (s, ν[C=C]).

Computational Details

DFT calculations were performed using ORCA2.9.1.[32] Large TZVP basis sets[33] were used throughout. The structures of the iron(II) complexes were optimized with the GGA functional BP86;[34] the absence of imaginary modes in numerical frequency calculations proved the optimized structures to be stationary points. Complexes were optimized in both their LS and HS states. Cartesian coordinates of all optimized structures are compiled in the Supporting Information (see Table S5–S28 in the SI). In order to assess the SCO energies, we used five derivatives of the well-established hybrid functional B3LYP[19,35] in single-point calculations. In these derivative functionals the amount of exact exchange a_0 has been varied stepwise from 0.20 (native B3LYP) to 0.00. Dispersion contributions were approximated using Grimme's DFT–D3 atom pairwise dispersion corrections of the parent B3LYP functional.[36] Solvent effects were accounted for in a dielectric continuum approach (COSMO),[37] parametrized for MeCN.

Acknowledgements

Financial supports from the German Research foundation (SFB840; project A10), the BayNAT program, and the University of Bayreuth are gratefully acknowledged. Open access funding enabled and organized by Projekt DEAL.

Keywords: Schiff base · Iron · Spin crossover · Density functional theory

[1] a) M. A. Halcrow (Ed.) *Spin-Crossover Materials*, John Wiley & Sons Ltd, Chichester **2013**; b) K. Senthil Kumar, M. Ruben, *Coord. Chem. Rev.* **2017**, *346*, 176–205; c) E. Coronado, *Nature Rev. Mater.* **2020**, *5*, 87–104; d) M. A. Halcrow, *Dalton Trans.* **2020**, *49*, 15560–15567; e) K. Senthil Kumar, Y. Bayeh, T. Gebretsadik, F. Elemo, M. Gebrezgiabher, M. Thomas, M.

Ruben, *Dalton Trans.* **2019**, *48*, 15321–15337; f) S. Brooker, *Chem. Soc. Rev.* **2015**, *44*, 2880–2892.
[2] M. A. Halcrow, I. Capel Berdiell, C. M. Pask, R. Kulmaczewski, *Inorg. Chem.* **2019**, *58*, 9811–9821.
[3] H. Kurz, J. Sander, B. Weber, *Z. Anorg. Allg. Chem.* **2020**, *646*, 800–807.
[4] M. Hostettler, K. W. Törnroos, D. Chernyshov, B. Vangdal, H.-B. Bürgi, *Angew. Chem. Int. Ed.* **2004**, *43*, 4589–4594; *Angew. Chem.* **2004**, *116*, 4689–4695.
[5] S. A. Barrett, C. A. Kilner, M. A. Halcrow, *Dalton Trans.* **2011**, *40*, 12021–12024.
[6] K. Cook, J. Laurence, R. Kulmaczewski, R. Mohammed, S. Dudley, S A. Barrett, M. A. Little, R. J. Deeth, M. A. Halcrow, *Angew. Chem. Int. Ed.* **2016**, *55*, 4327–4331; *Angew. Chem.* **2016**, *128*, 4399–4403.
[7] D. C. Ashley, E. Jakubikova, *Inorg. Chem.* **2018**, *57*, 9907–9917.
[8] S. C. C. van der Lubbe, P. Vermeeren, C. Fonseca Guerra, F. M. Bickelhaupt, *Chem. Eur. J.* **2020**, *26*, 15690–15699.
[9] B. Weber, E.-G. Jäger, *Eur. J. Inorg. Chem.* **2009**, *2009*, 465–477.
[10] B. Weber, *Coord. Chem. Rev.* **2009**, *253*, 2432–2449.
[11] S. Thallmair, W. Bauer, B. Weber, *Polyhedron* **2009**, *28*, 1796–1801.
[12] T. M. Pfaffeneder, S. Thallmair, W. Bauer, B. Weber, *New J. Chem.* **2011**, *35*, 691–700.
[13] W. Bauer, T. Ossiander, B. Weber, *Z. Naturforsch. B* **2010**, *2010*, 323–328.
[14] B. Weber, F. A. Walker, *Inorg. Chem.* **2007**, *46*, 6794–6803.
[15] B. Weber, E. Kaps, J. Weigand, C. Carbonera, J.-F. Létard, K. Achterhold, F. G. Parak, *Inorg. Chem.* **2008**, *47*, 487–496.
[16] H. Görls, E.-G. Jäger, *Cryst. Res. Technol.* **1991**, *26*, 349–355.
[17] H. Petzold, P. Djomgoue, G. Hörner, C. Lochenie, B. Weber, T. Rüffer, *Dalton Trans.* **2018**, *47*, 491–506.
[18] D. N. Bowman, E. Jakubikova, *Inorg. Chem.* **2012**, *51*, 6011–6019.
[19] M. Reiher, O. Salomon, B. Artur Hess, *Theor. Chem. Acc.* **2001**, *107*, 48–55.
[20] a) P. Stock, D. Wiedemann, H. Petzold, G. Hörner, *Inorganics* **2017**, *5*, 60; b) H. Petzold, G. Hörner, L. Schnaubelt, T. Rüffer, *Dalton Trans.* **2018**, *47*, 17257–17265.
[21] B. Weber, I. Käpplinger, H. Görls, E.-G. Jäger, *Eur. J. Inorg. Chem.* **2005**, *2005*, 2794–2811.
[22] a) H. Kurz, G. Hörner, B. Weber, *Z. Anorg. Allg. Chem.* **2020**, submitted; b) S. Schönfeld, K. Dankhoff, D. Baabe, M.-K. Zaretzke, M. Bröring, K. Schötz, A. Köhler, G. Hörner, B. Weber, *Inorg. Chem.* **2020**, *59*, 8320–8333.
[23] P. Gütlich, H. Goodwin (Eds.) *Topics in Current Chemistry*, *233–235*, Springer Berlin/Heidelberg **2004**.
[24] B. Weber, R. Betz, W. Bauer, S. Schlamp, *Z. Anorg. Allg. Chem.* **2011**, *637*, 102–107.
[25] A. Altomare, M. C. Burla, M. Camalli, G. L. Cascarano, C. Giacovazzo, A. Guagliardi, A. G. G. Moliterni, G. Polidori, R. Spagna, *J. Appl. Crystallogr.* **1999**, *32*, 115–119.
[26] a) G. Sheldrick, *Acta Crystallogr. Sect. A* **2008**, *64*, 112–122; b) G. Sheldrick, *SHELXL-97*, University of Göttingen, Göttingen, Germany **1997**.
[27] M. C. Burla, R. Caliandro, B. Carrozzini, G. L. Cascarano, C. Cuocci, C. Giacovazzo, M. Mallamo, A. Mazzone, G. Polidori, *J. Appl. Crystallogr.* **2015**, *48*, 306–309.
[28] G. M. Sheldrick, *Acta Crystallogr. Sect. C* **2015**, *71*, 3–8.
[29] a) C. K. Johnson, M. N. Burnett, *ORTEP-III*, Oak-Ridge National Laboratory, Oak-Ridge, TN **1996**; b) L. Farrugia, *J. Appl. Crystallogr.* **1997**, *30*, 565.
[30] C. F. Macrae, I. Sovago, S. J. Cottrell, P. T. A. Galek, P. McCabe, E. Pidcock, M. Platings, G. P. Shields, J. S. Stevens, M. Towler et al, *J. Appl. Crystallogr.* **2020**, *53*, 226–235.
[31] O. Kahn, *Molecular Magnetism*, VCH, New York, N.Y **1993**.
[32] F. Neese, *WIREs Comput. Mol. Sci.* **2012**, *2*, 73–78.
[33] A. Schäfer, H. Horn, R. Ahlrichs, *J. Chem. Phys.* **1992**, *97*, 2571–2577.
[34] D. A. Becke, *Phys. Rev. A* **1988**, *38*, 3098–3100.
[35] a) R. M. Dickson, A. D. Becke, *J. Chem. Phys.* **1993**, *99*, 3898–3905; b) B. Miehlich, A. Savin, H. Stoll, H. Preuss, *Chem. Phys. Lett.* **1989**, *157*, 200–206.
[36] S. Grimme, J. Antony, S. Ehrlich, H. Krieg, *J. Chem. Phys.* **2010**, *132*, 154104.
[37] A. Klamt, G. Schüürmann, *J. Chem. Soc. Perkin Trans. 2* **1993**, 799–805.

Manuscript received: November 2, 2020
Revised manuscript received: November 30, 2020
Accepted manuscript online: December 3, 2020